

Article

Facile Synthesis of Co_3O_4 Nanoparticle-Functionalized Mesoporous SiO_2 for Catalytic Degradation of Methylene Blue from Aqueous Solutions

Zhenlong Zha ¹, Wenjun Zhu ¹, Feng Chen ¹, Junchao Qian ¹ , Xiao-Qin Liu ², Lin-Bing Sun ², Zhengying Wu ^{1,*} and Zhigang Chen ¹

¹ Jiangsu Key Laboratory for Environment Functional Materials, School of Chemistry, Biology and Material Engineering, Suzhou University of Science and Technology, 1 Kerui Road, Suzhou 215009, China; BaconZ1996@163.com (Z.Z.); yxdzswj@163.com (W.Z.); chenfeng@mail.usts.edu.cn (F.Z.); ziyou1900@163.com (J.Q.); czg@usts.edu.cn (Z.C.)

² State Key Laboratory of Materials-Oriented Chemical Engineering, Nanjing Tech University, Nanjing 210009, China; liuxq@njtech.edu.cn (X.-Q.L.); lbsun@njtech.edu.cn (L.-B.S.)

* Correspondence: zyw@usts.edu.cn; Tel.: +86-512-67374120

Received: 19 August 2019; Accepted: 23 September 2019; Published: 27 September 2019



Abstract: In this study, a series of Co_3O_4 nanoparticle-functionalized mesoporous SiO_2 (Co-SiO_2) were successfully synthesized via a spontaneous infiltration route. Co species were firstly infiltrated into the confined spaces between the surfactant and silica walls, with the assistance of grinding $\text{CoCl}_2 \cdot 6\text{H}_2\text{O}$ and the as-prepared mesoporous SiO_2 . Then, Co_3O_4 nanoparticles (NPs) were formed and grown in the limited space of the mesopores, after calcination. Structures, morphologies, and compositions of the materials were characterized by X-ray diffraction, transmission electron microscopy, energy dispersion spectrum, N_2 adsorption, and Fourier transform infrared spectra. Results showed that the high content of Co ($r\text{Co:Si} = 0.17$) can be efficiently dispersed into the mesoporous SiO_2 as forms of Co_3O_4 NPs, and the structural ordering of the mesoporous SiO_2 was well-preserved at the same time. The Co_3O_4 NP functionalized mesoporous SiO_2 materials were used as Fenton-like catalysts for removing methylene blue (MB) from aqueous solutions. The catalyst prepared at $r\text{Co:Si} = 0.17$ could completely remove the high-concentration of MB ($120 \text{ mg} \cdot \text{L}^{-1}$), and also showed an excellent performance with a removal capacity of $138 \text{ mg} \cdot \text{g}^{-1}$ to $180 \text{ mg} \cdot \text{L}^{-1}$ of MB. Catalytic mechanisms were further revealed, based on the degradation results.

Keywords: mesoporous Co-SiO_2 ; adsorption; Fenton-like catalysis; methylene blue

1. Introduction

With the rapid increase in industrialization and urbanization, water pollution has become one of the major environmental threats to human health and ecosystems, over the last few decades [1]. Water pollution is broadly categorized into inorganic and organic. Organic pollutants, especially colored effluents, such as dyes and pigments, accumulate in lakes, rivers, and groundwater, causing serious harmful effects [2]. Various types of biological and physical methods have been utilized to remove organic compounds from industrial wastewater. Biological treatment is a cost-effective technology of removing organic dye from wastewater but suffers from some drawbacks, such as easy inactivation, owing to the toxic biological effects from organic chemicals [3]. Ion exchange or adsorption is also a common and effective means of removing organic pollutions. However, post-treatments are usually required to regenerate the resins/adsorbents and prevent secondary contamination [3]. Thus,

various alternative technologies are developed to solve such problems. Advanced oxidation processes (AOPs), which are effective in removing toxic and non-biodegradable substances from wastewater, have received worldwide attention [4,5]. Among the different kinds of AOPs, Fenton and Fenton-like reactions have been widely studied due to their high efficiency in generating hydroxyl radicals for decontamination of recalcitrant organic pollutants.

Conventional homogeneous Fenton catalysts are highly sensitive to solution pH and only exhibit a good catalytic performance within a narrow acidic condition range (pH = 2–3). Catalyst efficiency tends to decrease when the solution pH is increased [6]. Aside from their narrow pH range, the other disadvantages of conventional Fenton catalysts include extensive iron sludge formation, high operation cost, and difficult recovery. Therefore, dispersing the active catalytic sites on inorganic supports has become an alternative approach for constructing heterogeneous Fenton catalysts. Among various supports, ordered mesoporous silica is promising, due to its large specific area, adjustable pore structure, and satisfactory hydrothermal stability [7–10]. Metal or metal-oxide-loaded mesoporous SiO₂ materials have been widely utilized as heterogeneous catalysts for water treatment [11–16]. For example, a mesoporous Fe₂O₃–SiO₂ composite was feasibly synthesized and employed in methyl orange and methylene blue (MB) degradation [11,12]. The Cu nanoparticle-decorated Fe₃O₄–SiO₂ also has a rapid Fenton-like catalytic property for the oxidation of acetaminophen [13]. Other oxides, such as Cu, Mn, and bimetallic Cu–Fe oxides, can be loaded in mesoporous silica, serving as heterogeneous catalysts [14–16].

As one of the common transition metal oxides, cobalt oxide (Co₃O₄) also has Fenton-like catalytic property due to its variable valence state and redox capability [17]. In the reaction system, with coexisting Co species and H₂O₂, free radicals (·OH) are generated, thereby achieving the catalytic degradation of organic dye molecules, based on its strong oxidizing property [18]. Traditional impregnation is the most popular method to introduce Co species into mesoporous SiO₂. However, the Co species could not easily enter the mesopores and they tend to form oxide clusters on the outer surface of the mesoporous SiO₂, through impregnation [19]. This method could also lead to a partial structure collapse of the mesoporous material, resulting in a decreased catalytic performance [20]. Consequently, introducing the Co species into the pores of mesoporous SiO₂, without destroying the structural regularity of the material, remains a challenge in catalyst fabrication science.

In this study, a Co-modified mesoporous SiO₂ was fabricated through a spontaneous infiltration route. With the assistance of grinding, Co precursors were introduced and infiltrated into the confined space between the silica walls and the template. After the thermal decomposition of the Co precursors and the template, Co₃O₄ NPs were formed and highly dispersed on the mesoporous SiO₂ (Figure 1). The obtained Co₃O₄ NP-loaded mesoporous SiO₂ had a high Co content (*r*Co:Si = 0.17), and the ordered mesostructure was preserved. The synthesized Co₃O₄ NP-loaded mesoporous SiO₂ was used as a Fenton-like catalyst for removing organic dyes from wastewater.

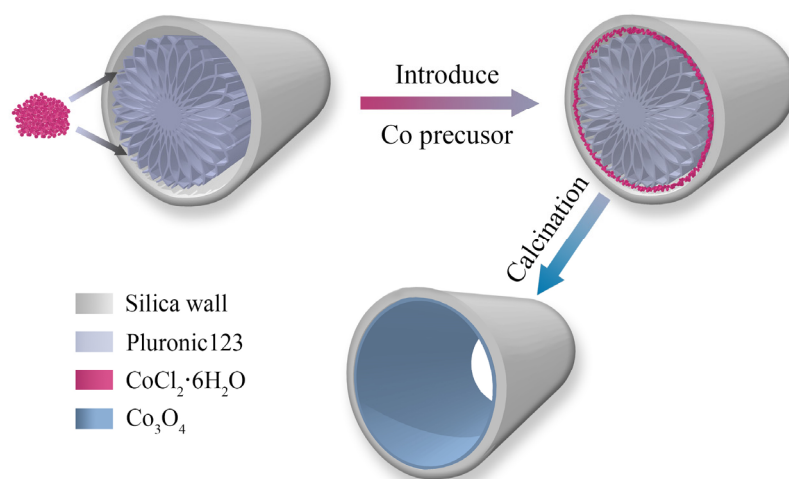


Figure 1. Schematic diagram of the synthetic process for Co–SiO₂ catalysts.

2. Results and Discussion

2.1. Structure and Surface Properties

The structure and surface properties of the synthesized catalysts were characterized via X-ray diffraction (XRD), N₂ adsorption–desorption isotherms, transmission electron microscopy (TEM) along with energy-dispersive X-ray spectroscopy (EDS), Fourier transform infrared (FTIR) spectra, and UV–visible diffuse reflectance spectra (UV–Vis DRS). Figure 2a shows the low-angle XRD patterns of the calcined mesoporous SiO₂ (labeled as mSiO₂) and the Co–SiO₂ catalysts, with different *r*Co:Si. All catalysts showed three well-resolved diffraction peaks of 0.85°, 1.44°, and 1.66° at 2θ. These peaks were indexed to (100), (110), and (200) reflections of the two-dimensional hexagonal mesostructure (space group *p6mm*), which is similar to the traditional mesoporous SBA-15 [16,21]. The intensity of the diffraction peak for the Co–SiO₂ catalysts was unchanged as Co content increased. Although a high amount of Co was introduced into the catalyst, the mesostructure order was well-preserved.

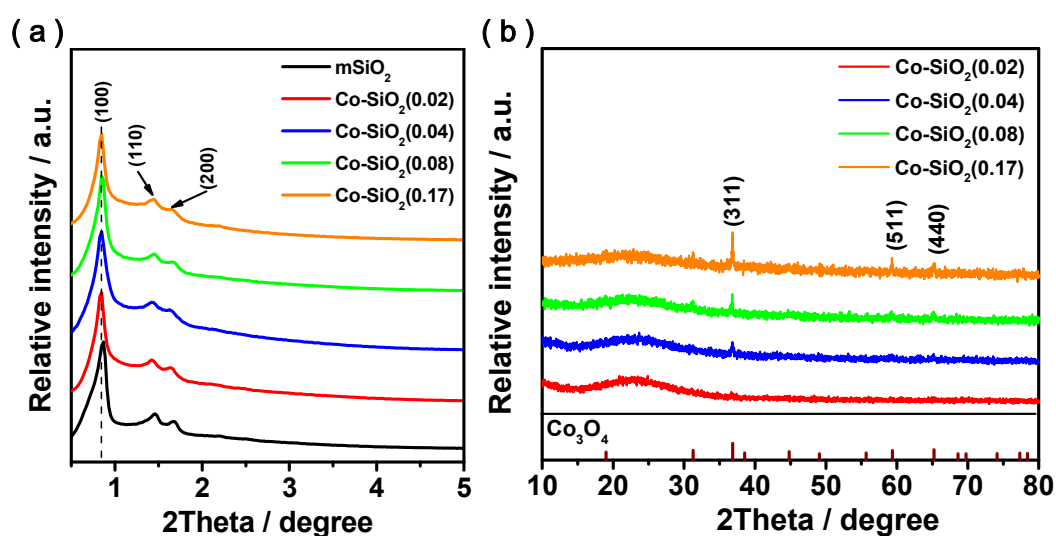


Figure 2. Low (a) and wide (b) angle XRD patterns of the mesoporous Co–SiO₂(*x*) catalysts.

Wide-angle XRD patterns (Figure 2b) showed that the mesoporous Co–SiO₂ catalyst with a low Co content has a diffraction peak centered at 23°, attributed to the amorphous SiO₂. When the Co content was increased to *r*Co:Si = 0.04, the obtained Co–SiO₂ (0.04) displayed an XRD peak at 2θ of 23° and a small peak at 36.8°, along with two dimly visible peaks at 59.4° and 65.2°, which were indexed to the (311), (511), and (440) reflections of the cubic Co₃O₄ (JCPDS No. 43-1003) [22]. Further raising the Co content to *r*Co:Si = 0.08 and 0.17, the intensity of the Co₃O₄ diffraction peaks raised and was still weak. The crystal size of the Co₃O₄ in the mesoporous SiO₂ calculated by Scherrer's equation (Equation (1)) was 4.6 nm. However, there were deviations by the Scherrer's equation caused by a broadening of the diffraction peaks when the calculated crystal size was very small [23]. So TEM was further used to observe the actual size of the Co₃O₄ NPs in the mesoporous SiO₂.

$$D = \frac{K\lambda}{B \cos \theta} \quad (1)$$

where *B* is the half peak width; 2θ is the diffraction angle; λ is the wavelength of the X-ray source applied, which was 1.54178 Å according to the Cu source that we used; *K* is a constant, which takes a value of 0.89; and *D* is the dimension of the crystallites as if they were cubes, monodispersed in size.

TEM images show the well-ordered periodic mesopores for the Co–SiO₂ (0.17) catalyst (Figure 3a). Moreover, no Co₃O₄ aggregates were observed from the TEM with high magnification (Figure 3 b), implying that Co₃O₄ could be highly dispersed on the catalyst. Prolonged exposure of the catalyst to the high-energy electron beam was further attempted, until the mesopores of the sample were corroded by

the electrons. Then, small nanoparticles with size between 3.3–6.2 nm (in the red circle) were observed (Figure 3c). EDS result confirmed the presence of a large number of Co in the Co–SiO₂ (0.17) catalyst (Figure 3d). The element mapping images verified that the Co species were successfully introduced into the mesopores of the Co–SiO₂ catalyst with a good dispersion (Figure 4). Macroscopic photographs also demonstrated uniform colors for the Co–SiO₂ catalysts. Co–SiO₂ (0.02) with the lowest Co content was light blue, Co–SiO₂ (0.04) was light gray–blue, and Co–SiO₂ (0.08) was slightly darker. With the highest Co content, Co–SiO₂ (0.17) was homogeneously purple (Figure S1). The uniform color of the four samples proved that the Co species were highly dispersed on the Co–SiO₂ catalyst.

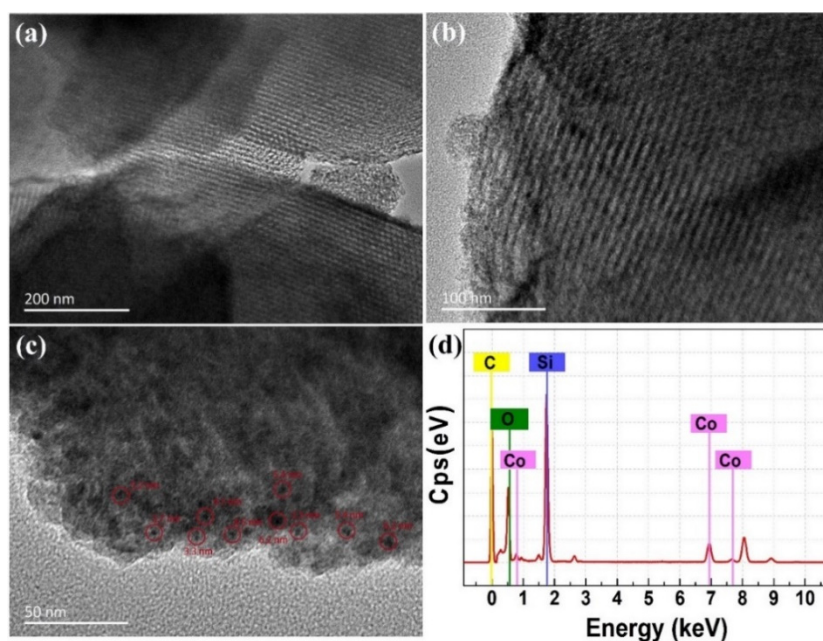


Figure 3. High resolution TEM (a,b), TEM of the sample exposed at prolonged electron beam (c) and EDS results (d) of the mesoporous Co–SiO₂ (0.17) catalyst.

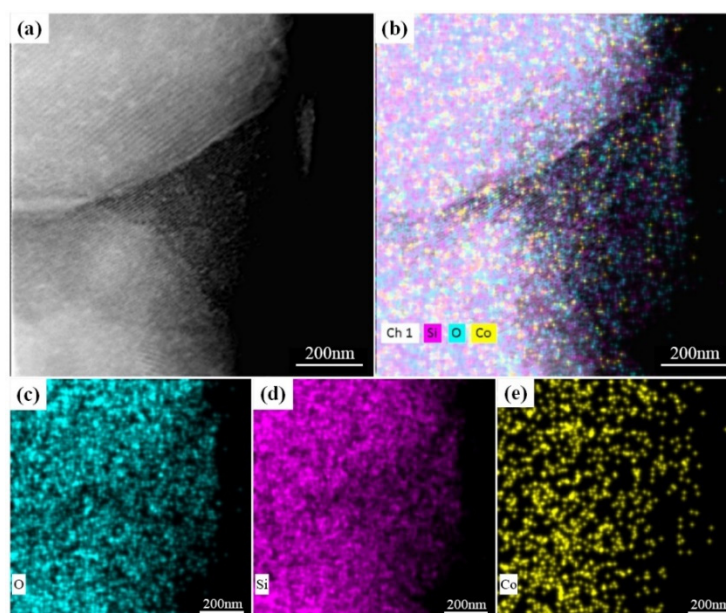


Figure 4. Dark-field TEM image (a) and an energy-dispersive X-ray spectroscopy (EDS) elemental mapping (b–e) of the Co–SiO₂ (0.17) catalyst.

Figure 5 shows the N_2 adsorption–desorption isotherms and pore size distributions (PSDs) of the Co–SiO₂ catalysts. The isotherms of all catalysts were of IV shape with H1-type hysteresis loops, indicating a regularly ordered straight channel similar to that of the conventional mesoporous SiO₂. The hysteresis loops of the Co–SiO₂ catalyst did not change remarkably, whereas the amount of adsorbed N_2 decreased slightly, following the increased Co content (Figure 5a). This result indicated that introducing the Co species via the spontaneous route had a negligible effect on the regularity of mesoporous channels [24]. PSD of the Co–SiO₂ catalysts was relatively narrow, as shown in Figure 5b. From Table 1, the specific surface area of the mesoporous Co–SiO₂ (586–444 m²·g^{−1}) was smaller than that of the support mSiO₂ (840 m²·g^{−1}), which could be attributed to the larger atomic weight of Co than that of Si [25]. The pore volume of the Co–SiO₂ (0.02) catalyst with less Co content was the same as that of the support. When the Co content increased, the pore volume of other Co–SiO₂ catalysts gradually decreased. Meanwhile, the primary pore size of all Co–SiO₂ catalysts was slightly smaller (9.23 nm) than that of the support (9.25 nm), but no remarkable changes were observed with an increase in the Co content. This result could be attributed to the existing states of Co in the catalysts. UV–Vis DRS and FTIR spectra could provide additional information on the chemical environment and the coordination nature of the Co species in the SiO₂ matrix [26].

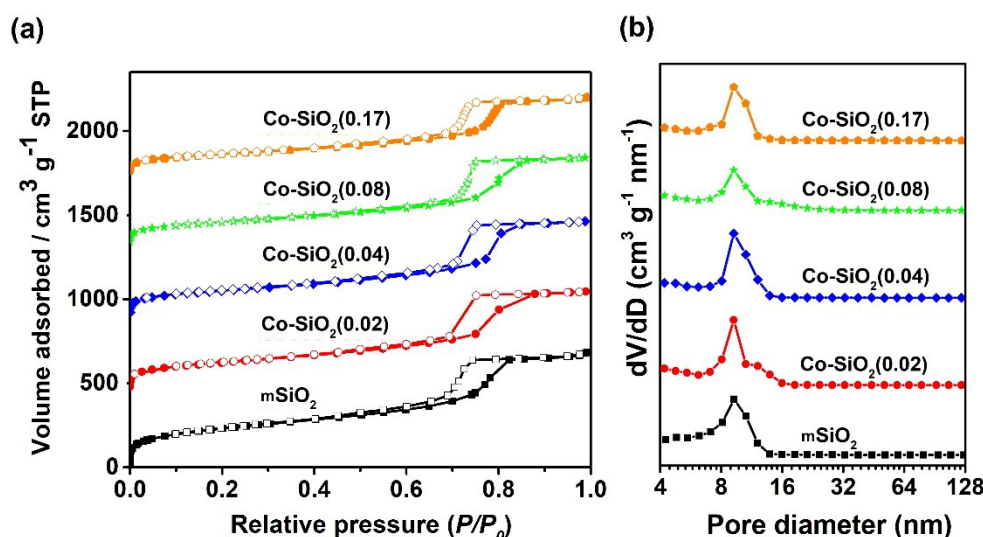


Figure 5. N_2 adsorption–desorption isotherms (a) and pore size distribution curves (b) of the mesoporous Co–SiO₂(*x*) catalysts.

Table 1. N_2 physisorption results of the mesoporous Co–SiO₂(*x*) catalysts.

Sample	a_0 (nm)	S_{BET} (m ² ·g ^{−1})	V_P (cm ³ ·g ^{−1})	D_{BJH} (nm)	W_d (nm)
mSiO ₂	11.75	840	0.91	9.25	2.50
Co–SiO ₂ (0.02)	12.03	586	0.91	9.23	2.80
Co–SiO ₂ (0.04)	12.03	542	0.87	9.23	2.80
Co–SiO ₂ (0.08)	12.03	497	0.81	9.23	2.80
Co–SiO ₂ (0.17)	12.03	444	0.71	9.23	2.80

Notes: a_0 : lattice parameter calculated from $a_0 = d_{100} * 2 / \sqrt{3}$; D_{BJH} : pore diameter calculated from the desorption branch; W_d : wall thickness calculated from $W_d = a_0 - D_{BJH}$.

Figure S2 shows the UV–Vis DRS of the mSiO₂ support and Co–SiO₂(*x*) catalysts. The mSiO₂ displays two weak absorption bands centered at 220 and 265 nm, which can be assigned to the absorption of SiO₂ [27]. The Co₃O₄ NP-functionalized samples exhibited broad absorption bands in the range of 200–800 nm. The adsorption intensity gradually increased with the Co content, indicating the complex oxidation and coordination states of the Co species in mSiO₂. The absorption between 200–300 nm (peak close to 200 nm) was attributed to a charge transfer between the oxygen ligands

and the central Co^{2+} ion in tetrahedral symmetry [28]. The weak absorption between 300–400 nm corresponded to the electronic transition of Co^{3+} ions in a disordered tetrahedral environment [29]. The absorption in the range of 400–600 nm (peaks centered at around 520 and 580 nm) could be assigned to the octahedral Co^{2+} ions. In addition, the absorption band at 600–800 nm (peaks at around 645 nm) indicated the presence of cobalt oxide nanoparticles in the form of Co_3O_4 , in which Co^{2+} ions were in a tetrahedral coordination and the Co^{3+} ions were in an octahedral position [30].

FTIR spectra of the mesoporous Co– SiO_2 catalysts and their precursors were thoroughly investigated to provide additional information on the interactions between the Co species and m SiO_2 support (Figure 6). Pristine $\text{CoCl}_2 \cdot 6\text{H}_2\text{O}$ showed characteristic bands at 3520, 3380, and 3170 cm^{-1} , which were ascribed to the absorption of CoCl_2 . The adsorption peak at around 1630 cm^{-1} was assigned to the stretching vibration of H_2O molecules, and bands below 1,000 cm^{-1} belonged to the fine structures of CoCl_2 [31,32] (Figure 6a). The absorption band that appeared near 802 cm^{-1} corresponded to the stretching vibration of Si–O–Si in the uncalcined sample SiO_2 –As [33], and the characteristic band near 960 cm^{-1} was attributed to the isolated silanol groups (Si–OH) [34]. The absorption bands appeared at around 2875–2960 cm^{-1} corresponding to the organic groups, such as $-\text{CH}_3$, $-\text{CH}_2-$, $\equiv\text{C}-\text{H}$, which mainly emerged from the organic templates in the SiO_2 –As sample. After the $\text{CoCl}_2 \cdot 6\text{H}_2\text{O}$ and SiO_2 –As were ground, the absorption bands at 3520, 3380, and 3170 cm^{-1} of $\text{CoCl}_2 \cdot 6\text{H}_2\text{O}$ in the obtained Co– SiO_2 (0.17)–As sample disappeared, indicating the strong interactions between $\text{CoCl}_2 \cdot 6\text{H}_2\text{O}$ and SiO_2 –As. After calcination, the characteristic absorption bands centered at 2875–2960 cm^{-1} of the organic template disappeared, whereas the peaks of Co–O appeared at 660 and 565 cm^{-1} [35] (Figure 6a). The intensities of such peaks were gradually enhanced due to the increasing Co content in the Co– SiO_2 catalysts. The stretching vibration band at 802 cm^{-1} corresponding to Si–O–Si was unchanged, whereas the band of Si–OH at 960 cm^{-1} weakened and finally disappeared in the Co– SiO_2 (0.17) sample (Figure 6b).

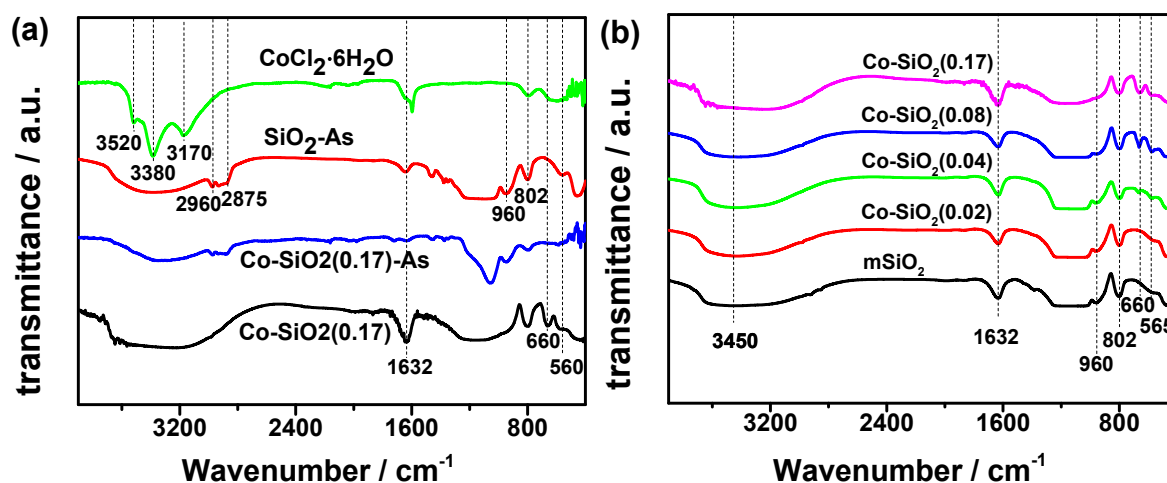


Figure 6. FTIR spectra of cobalt chloride hexahydrate; SiO_2 –As, the as-synthesized Co– SiO_2 (0.17)–As; and the calcined Co– SiO_2 (0.17) (a); the calcined m SiO_2 and the mesoporous Co– $\text{SiO}_2(x)$ catalysts (b).

2.2. Catalytic Performance

Figure 7 shows the adsorption and synergetic catalytic performance of different catalysts for removing the highly concentrated MB (120 $\text{mg} \cdot \text{L}^{-1}$) from aqueous solutions. For all catalysts, adsorption equilibrium was established within 6 h. The pristine m SiO_2 exhibited the highest capacity (89 $\text{mg} \cdot \text{g}^{-1}$), whereas pure Co_3O_4 showed an inconspicuous MB adsorption capability (6 $\text{mg} \cdot \text{g}^{-1}$). The synthesized Co_3O_4 NP-functionalized mesoporous SiO_2 (Co– SiO_2 (0.17)) could adsorb 86.4 $\text{mg} \cdot \text{g}^{-1}$ MB, which was negligibly lower than that of m SiO_2 but much higher than that of the simple mechanically mixed Co_3O_4 and m SiO_2 (named as mixed Co_3O_4 - SiO_2) (Figure 7a). After adsorption, H_2O_2 was introduced into the system at 6 h to initiate the catalytic reaction. There was an instant decline of

MB concentration in the catalyst-free system after the H_2O_2 addition, which was due to the solution dilution by the introduction of H_2O_2 . After that, no more obvious change on the MB concentration was observed (Figure 7a), suggesting that the interaction between MB and H_2O_2 was negligible. A similar phenomenon was observed in the control catalyst-free experiment, in which H_2O was added to the MB solution. The decrease of the MB concentration for the two catalyst-free systems with H_2O and H_2O_2 addition was almost the same (Figure 7a). Mesoporous mSiO_2 support did not exhibit a catalytic capability due to a lack of active sites. Pristine Co_3O_4 could degrade some MB molecules from the $120 \text{ mg}\cdot\text{L}^{-1}$ solution, but the total removal efficiency remained low (26%) due to its low adsorption capacity. The mixed $\text{Co}_3\text{O}_4\text{-SiO}_2$ also had a passable catalytic performance and could remove 79% of MB from the solution. In contrast to the pristine Co_3O_4 , mSiO_2 , and mixed $\text{Co}_3\text{O}_4\text{-SiO}_2$, the Co-SiO_2 (0.17) catalyst presented a remarkable catalytic capability and could completely remove MB from the solution (Figure 7b). This capability was attributed to the highly dispersed Co_3O_4 NPs on the mesoporous SiO_2 . Therefore, Co-SiO_2 (0.17) showed a significantly better MB removal efficiency than that of the mechanically mixed sample.

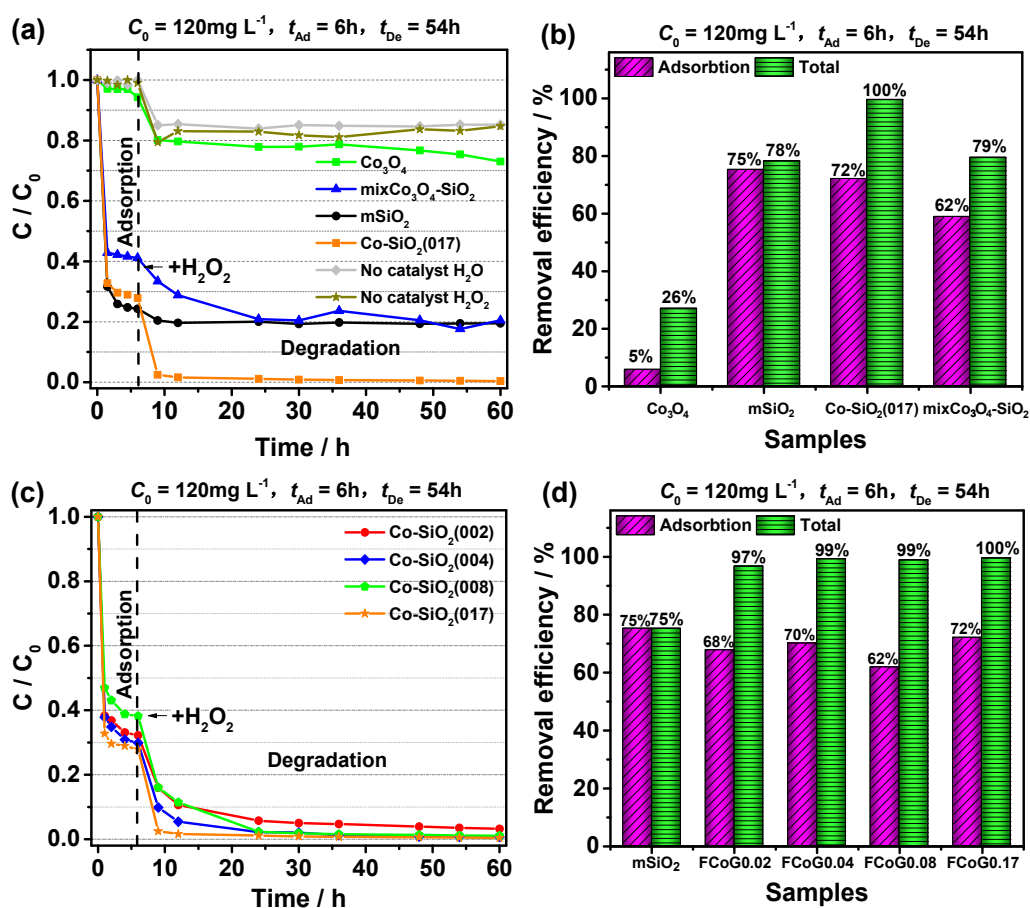


Figure 7. Adsorption and catalytic degradation (a) and the removal efficiency (b) of methylene blue (MB) by different catalysts. Adsorption and catalytic degradation (c) and the removal efficiency of MB (d) by the $\text{Co-SiO}_2(x)$ catalysts with different Co content.

The $\text{Co-SiO}_2(x)$ catalysts with different Co contents had a lower apparent MB adsorption amount ($71\text{--}82 \text{ mg}\cdot\text{g}^{-1}$) than the mSiO_2 support within 6 h. However, if we calculate the MB adsorption amount per S_{BET} , according to Equation (S1), it will be found that the introduction of the Co will increase the MB adsorption amount per S_{BET} of the catalyst (Table 2). Moreover, the adsorbed MB did not thoroughly occupy the surface of the catalyst. The MB molecule had a rectangular shape with dimensions $17 \text{ nm} \times 7.6 \text{ nm} \times 3.25 \text{ nm}$, and it was assumed that the MB molecule lays on its largest surface. Thus, the surface area covered by one MB molecule was approximately 130 nm^2 . Calculation

results showed that only 34%–47% of the Co–SiO₂ catalyst surface was covered by the MB molecules during the adsorption process (Equation (S2); Table 2). The enhanced MB adsorption amount per S_{BET} would be beneficial for the further catalytic degradation of MB molecules by the catalyst. As a result, all Co–SiO₂ catalysts exhibited better catalytic performance than the mSiO₂ and could remove almost all MB ($R \geq 97\%$) from the aqueous solution (Figure 7c,d).

Table 2. Theoretically calculated results for the adsorbed MB molecules occupied on the surface of the mesoporous Co–SiO₂(*x*) materials.

Sample	MB Adsorption Amount per $S_{BET}/(\text{mg}\cdot\text{m}^{-2})$	MB Occupied Percentage/%
mSiO ₂	0.11	26.9
Co–SiO ₂ (0.02)	0.14	34.2
Co–SiO ₂ (0.04)	0.15	36.7
Co–SiO ₂ (0.08)	0.16	39.1
Co–SiO ₂ (0.17)	0.19	46.5

Among the four Co–SiO₂ catalysts, Co–SiO₂ (0.17) presented the largest MB removal efficiency (100%), possibly due to the largest number of its active sites (Co). Furthermore, the catalytic degradation of MB was rapid within the initial 6 h after H₂O₂ introduction. The degradation rate then slowed down, and equilibrium was established at a total reaction time of approximately 30 h (Figure 7c). Co–SiO₂ (0.02) catalyst presented a relatively slower catalytic rate than that of other Co–SiO₂ catalysts. The pseudo-first-order reaction rate coefficient (*k*) of Co–SiO₂ (0.02) was 0.049, while that of the other Co–SiO₂ catalysts was considerably high (0.055–0.059), as shown in Figure 8a. As such, the highly dispersed Co₃O₄ NPs exhibited a good catalytic efficiency. MB solution is transparent but Co–SiO₂ (0.17) appeared blue at 60 h of reaction time (Figure 8b). This difference was attributed to the MB molecules adsorbed in the catalyst, which had not been thoroughly degraded at that time. The blue color of MB would finally disappear from the catalyst at prolonged reaction times.

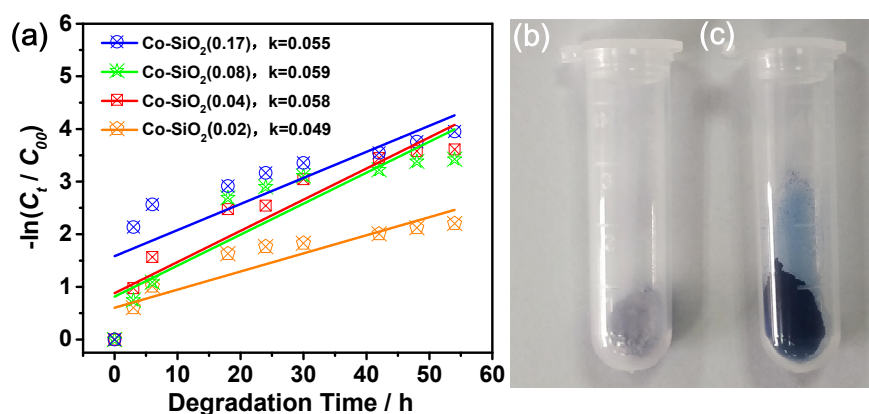


Figure 8. Kinetic curves of MB degraded by Co–SiO₂ catalysts (a) and photograph of Co–SiO₂ (0.17) catalyst before (b) and after (c) the catalytic experiment.

Figure 9 shows the adsorption/degradation of MB with different initial concentrations (C_0 , 80–180 mg·L^{−1}) by the Co–SiO₂ (0.17) catalyst. The adsorption amount of MB was 71 mg·g^{−1} at $C_{0(\text{MB})} = 80 \text{ mg}\cdot\text{L}^{-1}$ and was maintained at 78–81 mg·L^{−1} at $C_{0(\text{MB})} = 100\text{--}180 \text{ mg}\cdot\text{L}^{-1}$. However, the catalytic degradation amount of MB was enhanced when $C_{0(\text{MB})}$ was increased from 80 mg·L^{−1} to 150 mg·L^{−1}. The degradation amount of MB slightly increased when $C_{0(\text{MB})}$ was further increased to 180 mg·L^{−1}, indicating a weakened catalytic motivation in the highly concentrated MB solution.

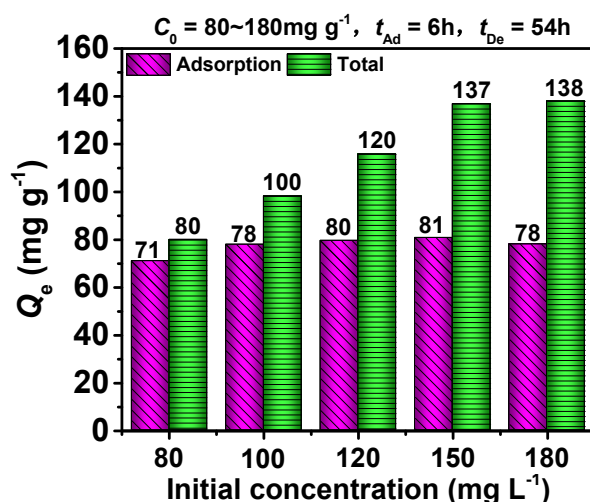


Figure 9. Effect of initial concentration on the degradation of MB by mesoporous Co-SiO₂ (0.17) catalyst.

The reusability of the catalyst was significant for its application. Therefore, the catalytic performance of Co-SiO₂ (0.17) in recycling experiments was evaluated. The initial concentration of MB was kept constant (120 mg·L⁻¹). After the adsorption and a catalytic reaction for 60 h, the catalyst was separated out of the solution, dried, calcined at 773 K for 2 h, and reused. It was observed that the total MB removal percentage decreased from 100% to 92% for the second run, and was maintained at 94% for the third run (Figure 10), implying that the Co-SiO₂ catalyst was stable in the recycling tests.

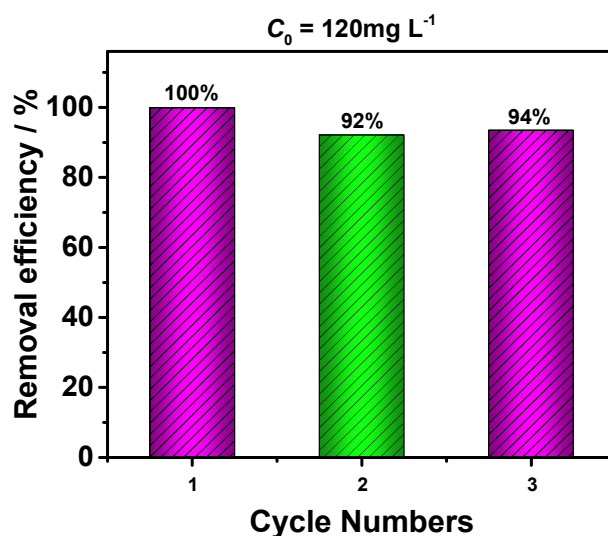


Figure 10. Recycling ability of the Co-SiO₂ (0.17) catalyst.

2.3. Mechanisms for the Degradation of MB

Figure 11 shows the UV-Vis spectra (200–800 nm) of the MB solution (120 mg·L⁻¹) degraded by the Co-SiO₂ (0.17) catalyst, over time. H₂O₂ was added to the reaction system to initiate the catalytic degradation of MB after 6 h of adsorption. Two characteristic absorption peaks at 665 and 614 nm were attributed to the chromophore functional groups of MB monomers and dimers. The other two peaks at 291 and 245 nm were ascribed to the π - π^* transitions related to unsaturated conjugated aromatic rings of MB [16]. The intensity of the absorption peak at 665 nm gradually decreased and shifted to the blue region (643 nm and lower wavelength), along with the reaction time variation from 6 h to 36 h (Figure 10). This finding could be attributed to the N-demethylation from MB [36]. The absorption peak at 614 nm also decayed and shifted to the blue regions (609 nm and lower). At 54 h of reaction

time, the absorption peaks of MB weakened, indicating the degradation of most MB in the solution by the Co-SiO₂ (0.17) catalyst. No new absorption peaks appeared during the reaction, suggesting that intermediate products that were difficult to degrade did not form in the system. The MB solution after catalytic degradation was centrifuged, and added to the clear Ca(OH)₂ solution. It was observed that the Ca(OH)₂ solution became a bit turbid, indicating the presence of CO₂ in the solution in which MB was degraded, as shown in Figure S3.

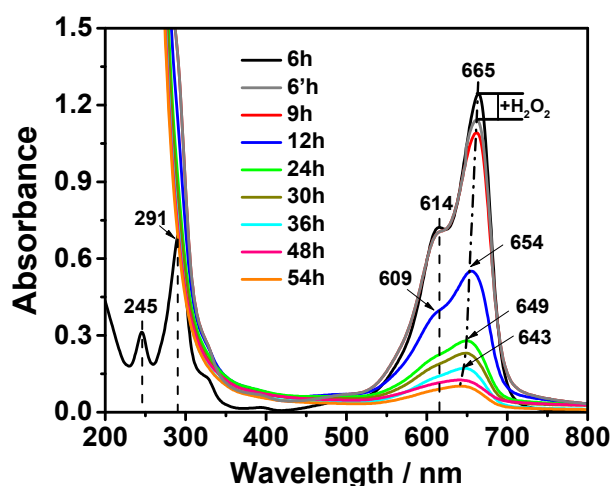
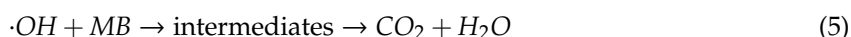
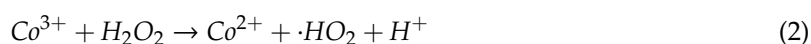


Figure 11. Temporal UV-Vis adsorption spectra of the MB solution during the degradation process in the Co-SiO₂ (0.17) and the H₂O₂ system.

Based on the above-mentioned catalytic results and the temporal UV-Vis absorption of the residual MB solution in the reaction process, a potential mechanism was proposed for decomposing MB by employing mesoporous Co-SiO₂ as the heterogeneous catalyst. MB molecules in the aqueous solution could initially be easily adsorbed into the mesopores, due to the high surface area and pore volume of the mesoporous Co-SiO₂ catalyst. After H₂O₂ was added, Co (II) and Co (III) species in the Co-SiO₂(x) might likely have catalyzed the H₂O₂ decomposition and produced ·HO₂ and ·OH. Then, the strongly oxidizing radicals could immediately attack the adsorbed MB molecules on the catalyst, thereby forming intermediate products. Finally, MB was degraded into H₂O and CO₂. Equations (2)–(5) show these specific reactions [37–39].



When the final product (H₂O and CO₂) was desorbed from the surface of the catalyst, the adsorption sites were regenerated and became available for the MB molecules. Then, the MB molecules in the solution would migrate to the adsorption sites again. The ·OH could attack the adsorbed MB molecule and degrade it to small and nontoxic inorganic molecules (Figure 12). In this reaction system, employing mesoporous Co-SiO₂ as a catalyst, the pH value of the solution changed from the original 6.8 to 5.3 at the end of the reaction. Thus, H⁺ was produced during the reaction, which was different from the conventional Fenton catalysis process. This phenomenon might be one of the reasons that the catalytic capability could be well-maintained under neutral conditions.

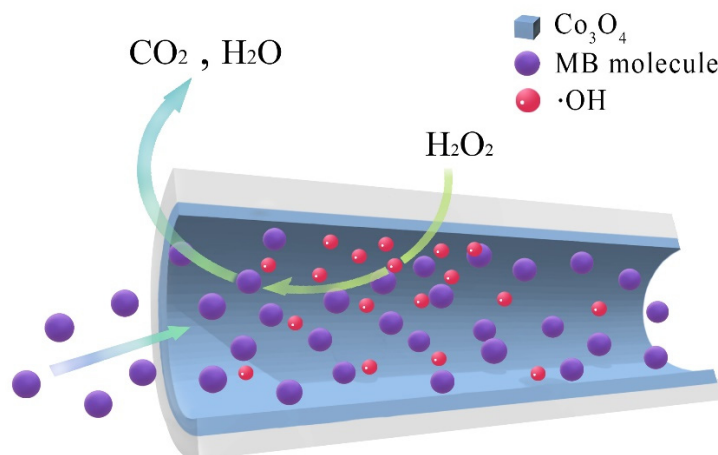


Figure 12. Schematic diagram of the MB adsorbed and degraded by the mesoporous Co-SiO₂ catalyst.

3. Materials and Methods

3.1. Synthesis of Co-SiO₂ Catalysts

Synthesis of the template-containing mesoporous SiO₂: Mesoporous SiO₂ was prepared according to the literature procedure, with a minor modification [21]. One gram of Pluronic P123 (Mw = 5800, EO₂₀PO₇₀EO₂₀) and 1.21 g of AlCl₃·6H₂O were dissolved in 37.5 g of H₂O at 308 K. Then 2.08 g of tetraethyl orthosilicate (TEOS) was added to the mixture. After that, the mixture was stirred under 308 K for 24 h and then heated at 373 K for another 24 h. Finally, the sample was filtered off, washed with water and air-dried. The obtained template-containing mesoporous SiO₂ was labeled SiO₂-As. Thermogravimetry (TG) result shows that the template and adsorbed water in the SiO₂-As sample were 40 wt. %, as shown in Figure S4.

Synthesis of Co₃O₄ NPs functionalized mesoporous Co-SiO₂ catalysts via the spontaneous infiltration route: A total of 0.6 g of SiO₂-As (including 6 mmol of SiO₂) and different amount (0.12, 0.24, 0.48, 1.00 mmol) of CoCl₂·6H₂O were mixed and manually ground for about 30 min to ensure that SiO₂-As and the Co species had adequately interacted with each other. Then, the mixture were calcinated at 550 °C for 5 h in a muffle furnace to remove the template and convert Co precursors into Co₃O₄ NPs. The resulting sample was denoted as Co-SiO₂(*x*) (*x* = rCo:Si), where *x* varied between 0.02, 0.04, 0.08, and 0.17.

3.2. Characterizations

The TG curves and DSC were obtained on a TA SDTQ-600 system. XRD patterns were recorded on a Bruker D8 Advanced diffractometer (Billerica, MA, USA) with Cu Kα radiator. N₂ adsorption-desorption isotherms were measured on a Micromeritics ASAP 2020 system. TEM and EDS were performed on a JEOL 2100F microscope (Tokyo, Japan) along with a Bruker XFlash-6T60 system. FTIR spectra were recorded on a Nicolet IS 10 spectrometer (Thermo, Waltham, MA, USA). UV-Vis DRS were measured on a T9CS UV-Vis spectrophotometer (Presee, Beijing, China).

3.3. Catalytic Experiments

Catalytic experiments were carried out by adding 0.15 g of catalyst into a 250 mL conical flask containing 150 mL of methylene blue (MB), with an initial concentration of 120 mg L⁻¹. The adsorption lasted for 6 h to ensure equilibrium. After this, 30 mL H₂O₂ was added to the system to initiate the catalytic reaction, according to the literature [40]. At different times, 2 mL of solution was taken out and centrifuged for measurements. Concentration of the MB solution was analyzed using a UV-Vis

spectrophotometer (Shimadzu, UV-2450). The removal efficiency of MB was calculated by an equation as below:

$$R = \frac{C_0 - C_t}{C_0} \quad (6)$$

where C_0 and C_t ($\text{mg}\cdot\text{L}^{-1}$) are the initial concentration of MB, and the concentration at different reaction time t (h), respectively.

The catalytic degradation curve was fitted by a pseudo-first-order kinetic model:

$$-\ln\left(\frac{C_t}{C_{00}}\right) = kt \quad (7)$$

where C_{00} ($\text{mg}\cdot\text{L}^{-1}$) is the initial MB concentration after the introduction of H_2O_2 ; k (h^{-1}) is the reaction rate coefficient.

MB with different initial concentrations (80~180 $\text{mg}\cdot\text{L}^{-1}$) was also used to detect the catalytic property of the Co-SiO₂ (0.17) sample. The total amount of MB adsorbed or degraded by the catalyst was calculated from the mass balance equation as follows:

$$Q_e = \frac{(C_0 - C_t)V}{M} \quad (8)$$

where Q_e ($\text{mg}\cdot\text{L}^{-1}$) is the amount of MB removed per gram of the catalyst; C_0 and C_e ($\text{mg}\cdot\text{L}^{-1}$) represent the initial and equilibrium concentration of MB. V (L) represents the volume of the MB solution, and M (g) represents the amount of the catalyst.

4. Conclusions

In summary, a facile grinding-assisted spontaneous infiltration route was employed to fabricate the Co-modified mesoporous SiO₂. Results showed that a strong interaction happened between the Co species and the template-containing mesoporous SiO₂ during the synthesis. Especially, this interaction and the confined space in the template and silica walls, are beneficial for the dispersion of Co species in SiO₂ support. Consequently, a large number of Co₃O₄ nanoparticles ($r_{\text{Co:Si}} = 0.17$) were efficiently introduced and highly dispersed in mesoporous SiO₂, without destroying the structural ordering. The surface area of the catalysts decreased, whereas the pore size remained unchanged when the Co content in the catalysts was increased. Due to the presence of a large amount of mesopores and Co catalytic sites, the Co-SiO₂ catalysts exhibited a satisfactory Fenton-like performance in catalytic degradation of MB in aqueous solutions. The typical catalyst Co-SiO₂ (0.17) presented an excellent removal efficiency to remove the high concentrated MB (120 $\text{mg}\cdot\text{L}^{-1}$). Moreover, the removal capacity of this catalyst to 180 $\text{mg}\cdot\text{L}^{-1}$ of MB reached 138 $\text{mg}\cdot\text{g}^{-1}$. Mechanisms showed that the good catalytic property of the mesoporous Co-SiO₂ was attributed to the large adsorption capability, as well as the highly dispersed Co catalytic sites of the catalyst. The present study revealed a facile way for the synthesis of functional materials for applications in adsorption/degradation of organic pollutants in aqueous solutions.

Supplementary Materials: The following are available online at <http://www.mdpi.com/2073-4344/9/10/809/s1>, Figure S1: Photographs of the mesoporous Co-SiO₂(x) catalysts: Co-SiO₂ (0.02) (a), Co-SiO₂ (0.04) (b), Co-SiO₂ (0.08) (c), and Co-SiO₂ (0.17) (d); Figure S2: UV-Vis DRS of the mesoporous Co-SiO₂(x) catalysts; Figure S3: Photographs of the solutions—clear Ca(OH)₂ (a,d,g), the clear supernatant (centrifuged MB solution after degradation) (b,e,h), mixed Ca(OH)₂ solution and the supernatant (c,f,i). (d,e,f) were taken under a flash light; (g,h,i) are magnified views of (d,e,f); Equation (S1) and (S2); Figure S4: TG in air and DSC curves of the template-containing SiO₂-As sample.

Author Contributions: Z.Z. and W.Z., catalysts preparation; F.C. and J.Q., catalysts characterization; X.-Q.L. and L.-B.S., catalytic experiments; Z.Z., writing—original draft preparation; Z.W. and Z.C., writing—review and editing.

Funding: This research was funded by the Natural Science Foundation (NSF) of the Jiangsu Province—Outstanding Youth Project (BK20180103), the Science and Technology Development Project of Suzhou (SYG201818), and the

NSF of the Jiangsu Province (BK20180971). Financial supports from the Jiangsu Collaborative Innovation Center of Technology and Material for Water Treatment, the Open Projects of the International Joint Laboratory of Chinese Education Ministry on Resource Chemistry (A-2017-002), the State Key Laboratory of Materials-Oriented Chemical Engineering (KL17-06), and the Suzhou Key Laboratory for Nanophotonic and Nanoelectronic Materials and Its Devices (SZS201812), are also gratefully acknowledged.

Conflicts of Interest: The authors declare no conflict of interest.

References

1. Sapkota, K.P.; Lee, I.; Hanif, M.A.; Islam, M.A.; Hahn, J.R. Solar-Light-Driven Efficient ZnO–Single-Walled Carbon Nanotube Photocatalyst for the Degradation of a Persistent Water Pollutant Organic Dye. *Catalysts* **2019**, *9*, 498. [[CrossRef](#)]
2. Samanta, P.; Desai, A.V.; Let, S.; Ghosh, S.K. Advanced Porous Materials for Sensing, Capture and Detoxification of Organic Pollutants toward Water Remediation. *ACS Sustain. Chem. Eng.* **2019**, *7*, 7456–7478. [[CrossRef](#)]
3. Dong, C.; Ji, J.; Shen, B.; Xing, M.; Zhang, J. Enhancement of H₂O₂ Decomposition by the Co-catalytic Effect of WS₂ on the Fenton Reaction for the Synchronous Reduction of Cr(VI) and Remediation of Phenol. *Environ. Sci. Technol.* **2018**, *52*, 11297–11308. [[CrossRef](#)] [[PubMed](#)]
4. Mahamuni, N.N.; Adewuyi, Y.G. Advanced oxidation processes (AOPs) involving ultrasound for waste water treatment: A review with emphasis on cost estimation. *Ultrason. Sonochem.* **2010**, *17*, 990–1003. [[CrossRef](#)] [[PubMed](#)]
5. Chan, S.H.S.; Yeong Wu, T.; Juan, J.C.; Teh, C.Y. Recent developments of metal oxide semiconductors as photocatalysts in advanced oxidation processes (AOPs) for treatment of dye waste-water. *J. Chem. Technol. Biotechnol.* **2011**, *86*, 1130–1158. [[CrossRef](#)]
6. Yang, C.; Wang, D.; Tang, Q. The synthesis of NdFeB magnetic activated carbon and its application in degradation of azo dye methyl orange by Fenton-like process. *J. Taiwan Inst. Chem. Eng.* **2014**, *45*, 2584–2589. [[CrossRef](#)]
7. Zhang, Z.; Balogh, D.; Wang, F.; Sung, S.Y.; Nechushtai, R.; Willner, I. Biocatalytic Release of an Anticancer Drug from Nucleic-Acids-Capped Mesoporous SiO₂ Using DNA or Molecular Biomarkers as Triggering Stimuli. *ACS Nano* **2013**, *7*, 8455–8468. [[CrossRef](#)]
8. Ding, M.; Huang, Y.; Guo, T.; Sun, L.-P.; Guan, B.-O. Mesoporous nanospheres functionalized optical microfiber biosensor for low concentration neurotransmitter detection. *Opt. Express* **2016**, *24*, 27152. [[CrossRef](#)]
9. Du, H.; Ma, L.; Liu, X.; Zhang, F.; Yang, X.; Wu, Y.; Zhang, J. A Novel Mesoporous SiO₂ Material with MCM-41 Structure from Coal Gangue: Preparation, Ethylenediamine Modification, and Adsorption Properties for CO₂ Capture. *Energy Fuels* **2018**, *32*, 5374–5385. [[CrossRef](#)]
10. Hong, Y.; Cha, B.J.; Kim, Y.D.; Seo, H.O. Mesoporous SiO₂ Particles Combined with Fe Oxide Nanoparticles as a Regenerative Methylene Blue Adsorbent. *ACS Omega* **2019**, *4*, 9745–9755. [[CrossRef](#)]
11. Han, Y.-F.; Chen, F.; Ramesh, K.; Zhong, Z.; Widjaja, E.; Chen, L. Preparation of nanosized Mn₃O₄/SBA-15 catalyst for complete oxidation of low concentration EtOH in aqueous solution with H₂O₂. *Appl. Catal. B Environ.* **2007**, *76*, 227–234. [[CrossRef](#)]
12. Panda, N.; Sahoo, H.; Mohapatra, S. Decolourization of Methyl Orange using Fenton-like mesoporous Fe(2)O(3)-SiO(2) composite. *J. Hazard. Mater.* **2011**, *185*, 359–365. [[CrossRef](#)] [[PubMed](#)]
13. Lyu, L.; Zhang, L.; Hu, C. Enhanced Fenton-like degradation of pharmaceuticals over framework copper species in copper-doped mesoporous silica microspheres. *Chem. Eng. J.* **2015**, *274*, 298–306. [[CrossRef](#)]
14. Li, X.; Kong, Y.; Zhou, S.; Wang, B. In situ incorporation of well-dispersed Cu-Fe oxides in the mesochannels of AMS and their utilization as catalysts towards the Fenton-like degradation of methylene blue. *J. Mater. Sci.* **2016**, *52*, 1432–1445. [[CrossRef](#)]
15. Do, Q.C.; Kim, D.-G.; Ko, S.-O. Catalytic activity enhancement of a Fe₃O₄@SiO₂ yolk-shell structure for oxidative degradation of acetaminophen by decoration with copper. *J. Clean. Prod.* **2018**, *172*, 1243–1253. [[CrossRef](#)]
16. Wu, Z.; Zhu, W.; Zhang, M.; Lin, Y.; Xu, N.; Chen, F.; Wang, D.; Chen, Z. Adsorption and Synergetic Fenton-like Degradation of Methylene Blue by a Novel Mesoporous α -Fe₂O₃/SiO₂ at Neutral pH. *Ind. Eng. Chem. Res.* **2018**, *57*, 5539–5549. [[CrossRef](#)]

17. Huang, Q.; Zhang, J.; He, Z.; Shi, P.; Qin, X.; Yao, W. Direct fabrication of lamellar self-supporting $\text{Co}_3\text{O}_4/\text{N}/\text{C}$ peroxymonosulfate activation catalysts for effective aniline degradation. *Chem. Eng. J.* **2017**, *313*, 1088–1098. [[CrossRef](#)]
18. Da'na, E.; Sayari, A. Adsorption of heavy metals on amine-functionalized SBA-15 prepared by co-condensation: Applications to real water samples. *Desalination* **2012**, *285*, 62–67. [[CrossRef](#)]
19. Xu, X.; Wu, J.; Xu, W.; He, M.; Fu, M.; Chen, L.; Zhu, A.; Ye, D. High-efficiency non-thermal plasma-catalysis of cobalt incorporated mesoporous MCM-41 for toluene removal. *Catal. Today* **2017**, *281*, 527–533. [[CrossRef](#)]
20. Martínez, A.N.; López, C.; Márquez, F.; Díaz, I. Fischer–Tropsch synthesis of hydrocarbons over mesoporous Co/SBA-15 catalysts: The influence of metal loading, cobalt precursor, and promoters. *J. Catal.* **2003**, *220*, 486–499. [[CrossRef](#)]
21. Wu, Z.Y.; Wang, H.J.; Zhuang, T.T.; Sun, L.B.; Wang, Y.M.; Zhu, J.H. Multiple Functionalization of Mesoporous Silica in One-Pot: Direct Synthesis of Aluminum-Containing Plugged SBA-15 from Aqueous Nitrate Solutions. *Adv. Funct. Mater.* **2008**, *18*, 82–94. [[CrossRef](#)]
22. Deng, J.; Kang, L.; Bai, G.; Li, Y.; Li, P.; Liu, X.; Yang, Y.; Gao, F.; Liang, W. Solution combustion synthesis of cobalt oxides (Co_3O_4 and $\text{Co}_3\text{O}_4/\text{CoO}$) nanoparticles as supercapacitor electrode materials. *Electrochim. Acta* **2014**, *132*, 127–135. [[CrossRef](#)]
23. Ungár, T. Microstructural parameters from X-ray diffraction peak broadening. *Scr. Mater.* **2004**, *51*, 777–781. [[CrossRef](#)]
24. Wang, C.; Lim, S.; Du, G.; Loebicki, C.Z.; Li, N.; Derrouiche, S.; Haller, G.L. Synthesis, Characterization, and Catalytic Performance of Highly Dispersed Co-SBA-15. *J. Phys. Chem. C* **2009**, *113*, 14863–14871. [[CrossRef](#)]
25. Hu, L.; Yang, X.; Dang, S. An easily recyclable Co/SBA-15 catalyst: Heterogeneous activation of peroxymonosulfate for the degradation of phenol in water. *Appl. Catal. B Environ.* **2011**, *102*, 19–26. [[CrossRef](#)]
26. Wojnarowicz, J.; Chudoba, T.; Koltsov, I.; Gierlotka, S.; Dworakowska, S.; Lojkowski, W. Size control mechanism of ZnO nanoparticles obtained in microwave solvothermal synthesis. *Nanotechnology* **2018**, *29*, 065601. [[CrossRef](#)]
27. Weckhuysen, B.M.; Schoonheydt, R.A. Recent progress in diffuse reflectance spectroscopy of supported metal oxide catalysts. *Catal. Today* **1999**, *49*, 441–451. [[CrossRef](#)]
28. Karthik, M. Characterization of Co,Al-MCM-41 and its activity in the t-butylation of phenol using isobutanol. *Appl. Catal. A Gen.* **2004**, *268*, 139–149. [[CrossRef](#)]
29. Somanathan, T.; Pandurangan, A.; Sathiyamoorthy, D. Catalytic influence of mesoporous Co-MCM-41 molecular sieves for the synthesis of SWNTs via CVD method. *J. Mol. Catal. A Chem.* **2006**, *256*, 193–199. [[CrossRef](#)]
30. Bhoware, S.S.; Shylesh, S.; Kamble, K.R.; Singh, A.P. Cobalt-containing hexagonal mesoporous molecular sieves (Co-HMS): Synthesis, characterization and catalytic activity in the oxidation reaction of ethylbenzene. *J. Mol. Catal. A Chem.* **2006**, *255*, 123–130. [[CrossRef](#)]
31. Abdelrazek, E.M.; Elashmawi, I.S. Characterization and physical properties of CoCl_2 filled polyethyl-methacrylate films. *Polym. Compos.* **2008**, *29*, 1036–1043. [[CrossRef](#)]
32. Teh, L.P.; Triwahyono, S.; Jalil, A.A.; Firmansyah, M.L.; Mamat, C.R.; Majid, Z.A. Fibrous silica mesoporous ZSM-5 for carbon monoxide methanation. *Appl. Catal. A Gen.* **2016**, *523*, 200–208. [[CrossRef](#)]
33. Siddiqui, Z.N.; Khan, K.; Ahmed, N. Nano Fibrous Silica Sulphuric Acid as an Efficient Catalyst for the Synthesis of β -Enaminone. *Catal. Lett.* **2014**, *144*, 623–632. [[CrossRef](#)]
34. Liotta, L. CoOx catalysts supported on alumina and alumina-baria: Influence of the support on the cobalt species and their activity in NO reduction by C_3H_6 in lean conditions. *Appl. Catal. A Gen.* **2003**, *245*, 167–177. [[CrossRef](#)]
35. Ali, G.A.M.; Fouad, O.A.; Makhoulouf, S.A. Structural, optical and electrical properties of sol-gel prepared mesoporous $\text{Co}_3\text{O}_4/\text{SiO}_2$ nanocomposites. *J. Alloy. Compd.* **2013**, *579*, 606–611. [[CrossRef](#)]
36. Zhang, T.; Oyama, T.; Aoshima, A.; Hidaka, H.; Zhao, J.; Serpone, N. Photooxidative N-demethylation of methylene blue in aqueous TiO_2 dispersions under UV irradiation. *J. Photochem. Photobiol. A Chem.* **2001**, *140*, 163–172. [[CrossRef](#)]
37. Ling, S.K.; Wang, S.; Peng, Y. Oxidative degradation of dyes in water using $\text{Co}^{2+}/\text{H}_2\text{O}_2$ and $\text{Co}^{2+}/\text{peroxymonosulfate}$. *J. Hazard. Mater.* **2010**, *178*, 385–389. [[CrossRef](#)]

38. Dong, J.; Song, L.; Yin, J.J.; He, W.; Wu, Y.; Gu, N.; Zhang, Y. Co(3)O(4) nanoparticles with multi-enzyme activities and their application in immunohistochemical assay. *ACS Appl. Mater. Interfaces* **2014**, *6*, 1959–1970. [[CrossRef](#)]
39. Chen, Y.; Pötschke, P.; Pionteck, J.; Voit, B.; Qi, H. Fe₃O₄ Nanoparticles Grown on Cellulose/GO Hydrogels as Advanced Catalytic Materials for the Heterogeneous Fenton-like Reaction. *ACS Omega* **2019**, *4*, 5117–5125. [[CrossRef](#)]
40. Wang, N.; Zheng, T.; Zhang, G.; Wang, P. A review on Fenton-like processes for organic wastewater treatment. *J. Environ. Chem. Eng.* **2016**, *4*, 762–787. [[CrossRef](#)]



© 2019 by the authors. Licensee MDPI, Basel, Switzerland. This article is an open access article distributed under the terms and conditions of the Creative Commons Attribution (CC BY) license (<http://creativecommons.org/licenses/by/4.0/>).